Experimental and numerical studies on the starting effect on the secondary flow in a bend

OLIVIER BOIRON, VALÉRIE DEPLANO
AND ROBERT PELISSIER

Equipe de Biomécanique Cardiovasculaire, IRPHE, UMR6594, Université de la
Méditerranée, Marseille, France

A numerical and experimental modelling study was carried out in a curved tube to analyse the behaviour of unsteady flows in a bend. Based on a test bench, with no mechanical disturbances, the flow behaviour was observed using fluorescein injection. Velocity measurements were performed using hot-film anemometry. In addition, a finite volume method was used to perform three-dimensional unsteady numerical simulations. Womersley parameter values between 8 and 21 and Dean number values between 110 and 420 were used to assess the parameters affecting the flow behaviour. Secondary motions were observed, experimentally and numerically, showing the complexity of the flow patterns. The initiation and subsequent development are explained quantitatively. Based on our analysis of the starting effect, the secondary patterns were found to be highly dependent on both the initial conditions and the flow waveforms.

1. Introduction

Unsteady flows through bends have been studied both experimentally and theoretically by many authors (see Berger, Talbot & Yao 1983). One of the main reasons for these studies is the fact that atherosclerosis is generated in the curvatures of large arteries such as the aorta and coronaries; atherosclerosis is responsible for nearly three-quarters of all deaths from cardiovascular disease. Several complex biomechanical mechanisms have been identified in the etiology of atheroma, including hemodynamic mechanisms. Caro, Fitzgerald & Schroter (1971), followed by Gessner (1973), Friedman *et al.* (1981) and Ku *et al.* (1985) have suggested that the sites at which this pathology develops are correlated with low oscillating wall shear stress values.

The spatial and temporal velocity profiles in the input regions are both decisive factors affecting fluid behaviour in bends. Previous studies can be broadly classified by whether they focus on fully developed or non-developed spatial flow patterns, or on oscillatory, pulsatile or physiological temporal flow patterns.

Non-developed flows are generally assumed to yield flat velocity profiles in the entrance of the bend, and their development depends on the inlet length and curvature effects. Flat velocity profiles can also occur temporarily in oscillatory flows at high frequency parameter values and in flows starting from rest. However, the spatial and temporal behaviour differ in the development of the boundary layer. In the aortic arch, the blood flow originating from a ventricular reservoir travels through the aortic

valve, starting from quasi-resting conditions (Parker 1977; Pedley 1980). The two main factors involved in this case are the entry length and the establishment of the flow.

All these flows are generally described in terms of non-dimensional parameters:

the Dean number: $De = (\widetilde{W}2a/\nu)\sqrt{a/R}$;

the Womersley parameter: $\alpha = a\sqrt{\omega/\nu}$;

the aspect ratio: $\delta = a/R$.

$\widetilde{W}$ is the average velocity during a cycle, a the tube radius, ν the kinematic viscosity of the fluid, ω the angular frequency of the oscillation and R the radius of curvature of the pipe.

In the case of fully developed oscillatory flows, Lyne (1971) obtained a perturbation solution for small Dean number values and large Womersley parameter values and established that, unlike steady flows, secondary structures are composed of two pairs of vortices called the Lyne circulation. This result was theoretically and experimentally confirmed by Zalosh & Nelson (1973), Bertelsen (1975), Munson (1975), Mullin & Greated (1980) and Eckmann & Grotberg (1988). In order to classify secondary flows for a wide range of Dean and Womersley number values, Sudo, Sumida & Yamane (1992) determined the Womersley number values experimentally and numerically in the physiological range ($\alpha = 5.5$–28). These authors suggested that secondary structures can be classified into five different groups, depending on their patterns: Dean circulation (type I), deformed Dean circulation (type II), circulation intermediate between Dean and Lyne (type III), deformed Lyne circulation (type IV) and Lyne circulation (type V).

In an experimental study using laser Doppler velocimetry on a pulsatile flow at the entry of a curved pipe, Talbot & Gong (1983) described the helical motions embedded in the Dean circulation and the three-dimensional separation observed at the inner wall. In order to mimic the characteristics of blood flows in an aortic arch, Naruse & Tanishita (1996) analysed the effects of large curvatures on pulsatile entrance flows in a curved tube. They established that the location of strong wall-shear oscillations corresponds to the vessel wall region where atherosclerosis frequently develops.

Several authors have considered the case of physiological waveforms. Chandran & Yearwood (1981), for example, performed an experimental study on a non-developed periodic physiological flow ($\alpha = 20.76$, $De = 320$) in a pipe with a low curvature ratio ($\delta = 0.1$). Using three-dimensional hot-film anemometry, these authors measured the axial, radial and tangential velocity components in different cross-sections of the bend. The spatial shape of the axial velocity profile at the inlet resembled an inviscid flow profile. These authors observed that the flow did not appear to be fully developed at points far (approximately eight diameters) from the entrance section. In addition, a reverse flow was found to occur at the inner wall during the diastolic phase of the cycle. As the fluid ran along the pipe, they also reported that the axial velocity maximum first shifted from the outer wall towards the inner wall in the middle of the tube in the upstream region, and then towards the outer wall, in the downstream region. These authors attributed this pattern to the combined effects of the reverse flow at the inner wall and the secondary flow occurring in the middle of the bend.

Yearwood & Chandran (1984) analysed the velocity profiles in a model for an human aortic arch, with the same entrance flow waveform as Chandran & Yearwood (1981) but with an aspect ratio $\delta = 0.4$, and their findings were in agreement with the numerical study by Chang & Tarbell (1985) focusing on the same physiological conditions.
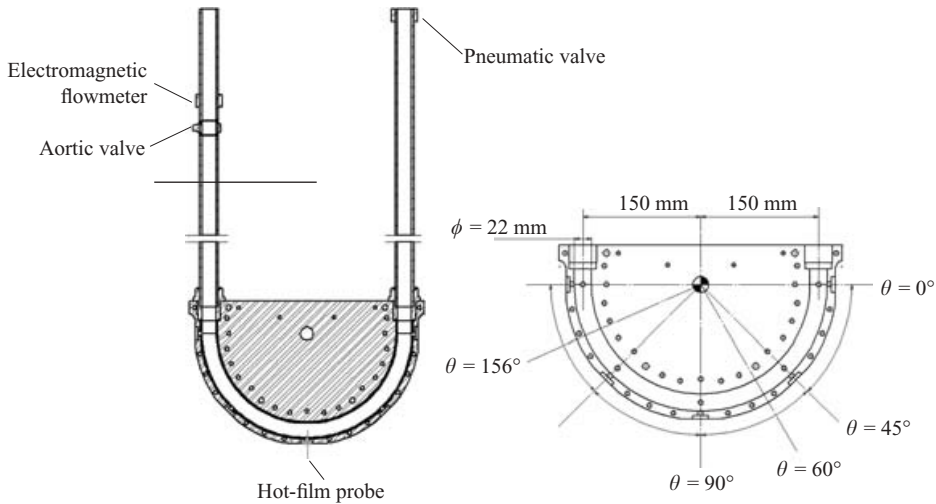
FIGURE 1. Experimental set-up.

Rindt *et al.* (1991) also examined a non developed periodic physiological flow at the entrance of a 90° curved tube. These authors concluded that, unlike in pulsatile flows, the diastolic phase has only a minor influence on the flow processes occurring in the systolic phase. In view of the fact that the blood flow in an aortic arch starts from quasi-rest conditions, Komai & Tanishita (1997) examined the case of a fully developed intermittent flow numerically, taking an intermittent parameter η to be the ratio between the systolic time and the entire period. This factor was found to range between 0 (a single pulse i.e. a starting/stopping flow) and $\frac{1}{2}$. For same values of this parameter, the flow continues to develop during the diastolic phase and does not completely vanish before the next systolic phase occurs. Owing to these residual flow structures, the secondary flows in the next systolic phase were found to be strongly affected by this process. At the same time, the maximum magnitude of the shear stress changed by less than 10% as η increased from 0 to $\frac{1}{2}$, but the slope of the time evolution was found to become steeper as η approached $\frac{1}{2}$.

Given the large body of literature on flows in bends and their relevance to atherosclerosis in terms of arterial wall shear stress evolution, the present study, in which three-dimensional starting/stopping flow is modelled experimentally and numerically, focuses on the following points. The velocity profiles and secondary flow patterns, will be described and their dependence on the initial hydrodynamic conditions will be analysed. Secondly, based on a quantitative analysis of the numerical results, we will focus on the interactions between the pressure and the inertial fields to elucidate the secondary flow evolution mechanisms.

2. Methods

2.1. *Experimental method*

2.1.1. *Geometrical model*

The experimental set-up used is shown in figure 1. Experiments were conducted in a U-shaped Plexiglas tube, 200 cm long with an internal radius a of 1.1 cm. The curved part was machined out of two halves of a Plexiglas sheet, which were polished
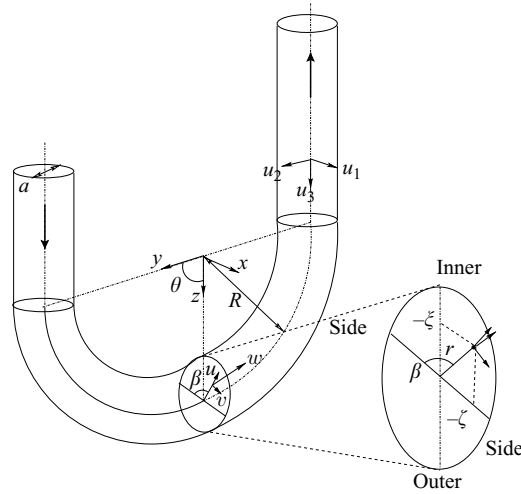
FIGURE 2. Coordinate systems and notations.

and then cemented together. With a constant radius of curvature R equal to 15 cm, we obtained an aspect ratio δ equal to 0.073. Holes were drilled in the curved part at the top of the sections corresponding to $\theta = 0°$, 45°, 90°, 135° and 180° to perform hot-film measurements (see figure 1).

Figure 2 gives the two coordinate systems used in this paper: Cartesian $(Oxyz)$ and toroidal $(\theta r \beta)$. In addition, we define two signed variables: $\xi = -r\sin\beta$ and $\zeta = -r\cos\beta$ for the inner to the outer diameter (called the transverse diameter) and the side to side diameter (called the perpendicular diameter), respectively, which vary from $-a$ to a.

2.1.2. *Set-up*

To avoid mechanical disturbances, we did not use a hydrodynamic generator but simply analysed the oscillations of a fluid column under the influence of gravity. The fluid was initially loaded into one branch of the U-tube and the motion of the fluid was then triggered by a pneumatic valve connected to the atmosphere. Based on inviscid fluid theory, it can be shown that the oscillation period, $T = 2\pi\sqrt{\ell/2g}$, depends only on the length, ℓ, of the fluid column in the tube. In order to reduce ℓ, adjust the period and exactly tune the acceleration and deceleration times, we controlled the time lag in the opening of the pneumatic valve. To stop the oscillations and model physiological flows, an aortic valve (Carpentier-Edwards model 2625) was placed in one of the branches. We then obtained a single oscillation corresponding to the required starting/stopping flow. The total volume, V, of liquid in the U-tube was about 1.45 l, corresponding to $\ell \approx 3.81$ m. The initial load, $\Delta\ell$, varied from 0.1 m to 0.3 m. The distances from the free surfaces to the inlet and outlet bend sections were greater than 50 tube diameters.

The fluid used in this experiment was an aqueous glycerol solution with various volume fractions of water. The viscosity was measured at room temperature. Viscosity values of 1, 3.9 and 7 cP were obtained with pure water and with 20% and 40% volume fraction of glycerol solutions respectively. The laboratory temperature was kept constant throughout the experiments.

2.1.3. *Measurements*

Quantitative data were obtained by measuring the flow rates and the velocities. The instantaneous flow rate signal was recorded downstream from the aortic valve by means of an electromagnetic blood flowmeter (Gould Statham SP2202). The velocity measurements were performed with a hot-film straight velocity probe 55R11 operating with a Dantec 90C10 constant-temperature anemometer. These signals were digitized and then recorded on a computer using a National Instruments ATMIO16E10 acquisition board.

The DANTEC 55R11 hot-film probe has a diameter of $0.75\,\mu\text{m}$ and an overall length of 3 mm. It was introduced into the bend through holes fitted with a special probe carrier ensuring that it was at the right position and orientation. The hot-film prove was mounted in the bend in such a way that its axis was perpendicular to that of the tube.

Qualitative data on the secondary motions developing in the bend were obtained using the classical slice laser (argon ion laser, $\lambda = 488\,\text{nm}$) technique. Fluorescein was injected at the wall upstream from the visualization plane. The flow motion was recorded by means of a video camera recorder equipped with a macro lens.

2.1.4. *Calibration*

The dynamic calibration of the hot-film probe was carried out on a fully developed unsteady laminar flow in a straight pipe. The pipe, 4 m in length and 2.2 cm in internal diameter was connected to a computer-controlled hydrodynamic generator to obtain the required flow rate. With this flow, the axial velocity values can be calculated from the mesured flow rate using a simple numerical model. In a cylindrical coordinate system, the axial velocity component, w, is obtained by solving

$$\frac{\partial w}{\partial t} + \frac{1}{\rho}\frac{\partial p}{\partial z} - \frac{\nu}{r}\frac{\partial}{\partial r}\left(r\frac{\partial w}{\partial r}\right) = 0, \tag{2.1}$$

with the following initial and boundary conditions:

$$\frac{\partial w}{\partial r}\Big|_{r=0,t} = 0, \tag{2.2}$$

$$w|_{r=a,t} = 0, \tag{2.3}$$

$$w|_{r,t=0} = 0. \tag{2.4}$$

The axial pressure gradient can be determined at any time from the flow rate recorded, using a shooting method. Equation (2.1) is discretized using a Crank–Nicholson scheme. Using this procedure, we deduce a ten-order polynomial calibration law that fits the experimental data. The effective cooling velocity U_{eff} is obtained in line with Jørgensen (1971) from $U_{eff}^2 = U_N^2 + kU_T^2 + hU_B^2$. Assuming ideal yaw and pitch factors, $k = 0$ and $h = 1$ respectively, the effective cooling velocity corresponds to the velocity component perpendicular to the sensor. The $k = 0$ hypothesis introduces an error of only 1%, which is good given the small values of the tangential velocity component.

The electromagnetic flowmeter was calibrated by measuring the fluid volume crossing it during a given time. The precision was about $0.1\,\text{l min}^{-1}$. A 100 Hz built-in low-pass filter was used for all the measurements.

2.1.5. *Hydrodynamic parameters*

Since $\delta = 0.073$ is constant, the flow behaviour depends on two non-dimensional parameters: the Dean number, De, and the frequency parameter, α. These parameters are calculated using the systolic time T_s as the time scale. The systole is normally

Case	ρ (kg m^{-3})	μ (cP)	De	α	T_s (s)	V (l)	Δl (m)
1	1100	7	110	8	1.85	1.45	0.15
2	1100	7	221	8.33	1.72	1.45	0.315
3	1065	3.9	346	10.95	1.73	1.45	0.285
4	1085	3.4	301	12.84	1.47	1.25	0.3
5	1000	1	423	21.5	1.64	1.45	0.1

TABLE 1. Classification of the hydrodynamic tests.
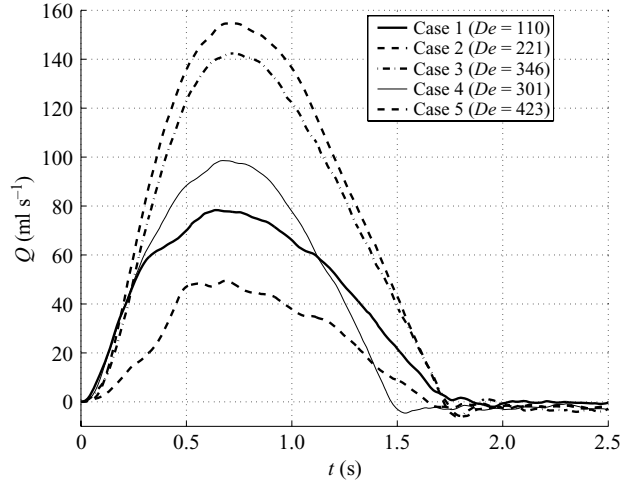
FIGURE 3. Flow rate waveforms.

defined as the ventricular ejection time equivalent to the first third of the cardiac period. The systole ends when the aortic valve closes, which corresponds to the onset of the flow deceleration. In this paper, the systole is defined as the time during which the flow rate differs from zero.

Associating a time scale with the cardiac period is not an appropriate means of analysing the flow dynamics because we are dealing here with a single pulse. In addition, the hydrodynamic behaviour depends on the acceleration and decceleration times, and in line with Komai & Tanishita (1997), we therefore define a time scale using these two values.

Several cases were studied, with various experimental viscosities and five of them, which are summarized in table 1, are presented here. The flow rate waveforms are given in figure 3.

2.2. *Numerical method*

The solutions of the three-dimensional unsteady Navier–Stokes and continuity equations were obtained for the case of a laminar flow in a rigid curved tube using the FLUENT software package.

2.2.1. *Geometrical and physical models*

The geometrical model used had the same caracteristics as the experimental one (figure 1). The walls are rigid and non-porous. The fluid is assumed to be Newtonian and its physical properties are constant in space and in time. Therefore, the governing

equations, in a Cartesian coordinates system, are given by

$$\nabla \cdot \boldsymbol{u} = 0, \tag{2.5}$$

$$\frac{\partial \boldsymbol{u}}{\partial t} + \boldsymbol{u} \cdot \nabla \boldsymbol{u} = -\frac{1}{\rho} \nabla p + \nu \Delta \boldsymbol{u}, \tag{2.6}$$

where $\boldsymbol{u}$ is the velocity vector, p the static pressure, t the time, ν the kinematic viscosity and ρ the density.

2.2.2. *Boundary and initial conditions*

Along the walls, we apply the usual no-slip velocity conditions. At the tube entrance, experimental flow conditions based on the flow rates recorded are imposed, represented by their axial velocity profiles. The inlet length is equal to ten radii. At the outlet, which is located twenty radii from the bend outlet, we assume a zero normal gradient for all the flow variables except the pressure. At $t = 0$ s, the fluid is assumed to be at rest.

2.2.3. *Numerical model*

The set of equations (2.5) and (2.6) is nonlinear and time dependent. The Fluent package solves these governing equations using the finite volumes method. For the convection terms in equation (2.6), a second-order upwind scheme is used to interpolate the face values of the various quantities from the cell centre values. The diffusion terms are central differenced and are always second-order accurate. The temporal discretization involves integrating all the terms in the differential equations with a time step Δt. The integration of the transient terms is implicit using a second-order formulation. The PISO algorithm is used to link pressure and velocity. The discretized equations are then solved sequentially using a segregated solver. Convergence is obtained when the residual reaches at least 10^{-5} for the pressure and 10^{-8} for the three velocity components. As in the experiment, we take only one flow pulse. For further details of the time and spatial discretization schemes and residuals see Fluent (1998).

2.2.4. *Grid refinement.*

The grids used for the numerical simulations consist of hexahedral elements. They are obtained by sweeping the mesh node pattern of a specified source face through the volume along a bend generator line. The source-face grid contains only quadrilateral elements.

Stokes layer thickness and wall refinement

Unsteady flow at high α values results in steep velocity gradients close to the walls, which requires a non-uniform grid in the radial direction, and a finer grid spacing near the wall. The distance from the first cell to the tube wall must correspond to the Stokes layer thickness, δ_s, in which the viscous effects are confined. Pelissier (1972) has determined a semi-analytical way of describing the evolution of the ratio δ_s/a for a fully developed flow in a straight tube, starting at rest and moving under the influence of a sinusoidal longitudinal pressure gradient. With a flow of this kind and $\alpha > 5$, Pelissier established, for a given t, three laws depending on the reduced time variable ωt:

   (i) if $\omega t \geqslant 1$: $\delta_s^t/a = 5\alpha^{-1.56} \mathrm{e}^{-0.35\sqrt{\omega t}}$;

   (ii) if $0.04 < \omega t < 1$: $\delta_s^t/a = 5\alpha^{-2.3} \mathrm{e}^{-0.7\sqrt{\omega t}}$;

   (iii) if $\omega t \leqslant 0.04$: $\delta_s^t/a = (20/\alpha^2)\sqrt{\omega t}$.

Case	1	2	3	4	5
α	8	8.33	10.95	12.84	21.5
$\delta_s^{\Delta t}/a$	0.029	0.028	0.016	0.0125	0.0042

TABLE 2. Stokes layer thickness.

Δt	0.01 s	0.05 s	0.1 s
12 cells	1.58×10^{-4}	1.66×10^{-4}	2.69×10^{-4}
14 cells	0.55×10^{-4}	0.55×10^{-4}	1.24×10^{-4}
24 cells	0.52×10^{-4}	0.65×10^{-4}	0.86×10^{-4}

TABLE 3. Error versus time step with various meshes.

In the first computational time step, we obtain, with $t \approx \Delta t$:

$$\frac{\delta_s^{\Delta t}}{a} \sim \frac{20}{\alpha^2} \sqrt{\omega \Delta t}. \tag{2.7}$$

Table 2 gives the values of the ratio $\delta_s^{\Delta t}/a$ for the various simulations and a time step $\Delta t = 2.510^{-3}$ s. With the smallest Stokes layer thickness, corresponding to case 5, $\alpha = 21.5$, this ratio is 0.0042. This value is obtained for a straight tube; it gives a guideline for choosing the distance from the first cell to the tube wall for the bend model.

Tests on the number of cells in the radial direction and the time-step value

Several tests were performed in a straight tube to determine the optimum grid. The time step was then fixed by performing convergence tests on the grids. Three surface grids are used with an increasing number of cells per radius: 12, 16 and 24. The size of the first cell remains fixed and identical in all three cases (see the previous subsection). The number of cells on the circumference is fixed at 48 for all three grids.

To determine the number of cells required in the radial direction, we take a cylindrical straight tube and simulate a fully developed flow starting at rest and moving under the influence of a sinusoidal longitudinal pressure gradient. The frequency parameter is that in case 3 ($\alpha = 10.95$, $Re = 1270$). The number of cells in the longitudinal direction is not of great importance once the flow has developed. The grid spacing is therefore uniform in this direction, and we take it to be 10^{-3} m. This model has the advantage of having a known analytical solution (Avula 1969), to which the solutions resulting from the simulation can thus be compared. To determine the accuracy of the numerical solution we calculate the relative quadratic error of the velocity with the analytical solution over the whole field. The evolution of the error is shown for the three grids in table 3 at a given time during the acceleration according to the time step Δt. The time steps tested are $\Delta t = 0.01$ s, 0.05 s, 0.1 s.

The finest grids, i.e. 16 and 24 cells on the radius, show similar behaviour and converge with a residual level of about 5×10^{-5} at time steps smaller than 0.05 s, and at time steps smaller than 0.05 s, the error no longer decreases. The limits of the spatial discretization have therefore been reached.

Based on these tests, 21 cells were used on the radius with a time step of $\Delta t = 2.5 \times 10^{-3}$ s. The surface grid used, having 21 cells on the radius, 48 cells on the circumference and the first cell located 5×10^{-5} m from the wall, is shown in figure 4.
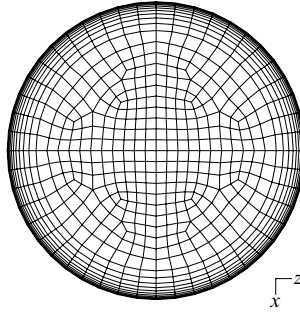
FIGURE 4. Face mesh.

Tests on the number of cells in the longitudinal direction

Based on the three previously determined parameters, namely the size of the first cell, the number of cells on the radius and the time step, we then tested the number of cells in the longitudinal direction. For this purpose, it was necessary to use a tube with a bend. The grid spacing is constant in this direction. We test various spacings : coarse : 0.0028 m, medium : 0.0014 m and fine : 0.00072 m i.e. 38, 76 and 152 cells respectively, for a length of 10 radii. The hydrodynamic conditions are those of case 3 ($\alpha = 10.95$, $De = 346$). As there is no analytical solution for this situation, we compared the results for the three grids at a given time of the simulation ($t = 0.35$ s). We calculated the relative quadratic error of the longitudinal velocity component u_3 along the axis of the bend ($r = 0$), taking for reference the results obtained with the finest grid. We found an error of less than 5×10^{-4} for the medium grid and about 10^{-3} for the coarse one. Therefore we chose the medium grid with 76 cells for 10 radii. These tests also confirmed that the inlet length of ten radii used was sufficiently large.

The final grid consisted of 451 472 elements and the grid refinement procedure yielded grid-independent velocity fields.

3. Results and discussion

To check the reliability of our numerical results, we first compared the velocity profiles resulting from our simulations with those obtained from hot-film anemometry measurements averaged over 50 realizations. We then made qualitatively comparisons between the computed flow structures in several cross-sections of the bend and the flow visualizations (see § 3.2).

3.1. *Velocity profiles*

The velocity profiles along the transverse diameter are plotted for case 4 in figure 5. Error bars for the experimental data are absolute errors.

The numerical and experimental results were found to be in relatively good agreement. At the beginning of the acceleration phase, $t = 0.3$ s, the maximum velocity is located near the inner wall. As the flow becomes rotational, the velocity peak moves towards the outer wall during the deceleration phase, $t = 1$ s. At $t = 1.3$ s, reversed flow develops at the inner wall as the result of the stopping effect, as described by Weinbaum & Parker (1975).
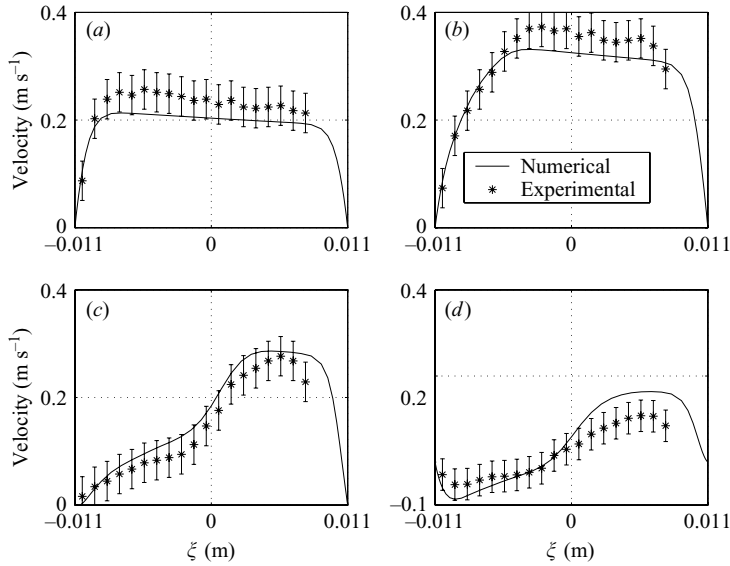
FIGURE 5. Velocity profiles along transverse diameter at $\theta = 90°$, case 4. Numerical compared to experimental. (*a*) $t = 0.3$ s, (*b*) 0.6 s, (*c*) 1 s, (*d*) 1.3 s.

During the early acceleration phase, the skewing of the velocity maximum towards the inner wall was previously observed by Yearwood & Chandran (1984) at the apex of their aorta model (i.e. corresponding approximately to our $\theta = 90°$ cross-section).

3.2. *Analysis of the secondary flow patterns*

Instantaneous secondary flows obtained from the numerical computations are shown in figures 6, 12, 15 in the $\theta = 90°$ bend cross-section, corresponding to cases 1, 2 and 5 (see table 1 for details). The vectors are plotted at the mesh cell centres.

At relatively low Dean numbers and frequency parameter values (case 1: $De = 110$, $\alpha = 8$, figure 6) a viscous layer can be observed during the acceleration ($t = 0.2$ s) along the lateral walls, which leads to two circumferential rolls inside this layer. These motions are directed from the outer wall towards the inner wall. At the same time, two weak contra-rotating vortices appear. These bean-shaped vortices are located close to the lateral walls, circumventing the potential core at the tube centre. The vortex cores are located close to the equatorial plane ($\beta = 180°$).

At the end of the acceleration phase ($0.5 \leqslant t \leqslant 0.65$ s), the contra-rotating vortices expand radially until they occupy almost the whole section. Their cores are located in the upper part of the cross-section. A strong jet-like motion across the centre of the tube develops from the inner towards the outer wall.

These secondary structures are associated with flat axial velocity profiles along the perpendicular diameter (figure 7, $t \leqslant 0.65$ s). Along the transverse diameter, the axial velocity maximum occurring at the inner wall at $t \leqslant 0.65$ s is shown in figure 8(*a*). The radial velocity profiles observed along the transverse diameter (figure 9, $t \leqslant 0.65$ s) show weak values reaching a maximum of only 4% of the axial velocity values.

To quantify the amplitude and the temporal evolution of the circumferential rolls we plot (figure 10) the maximum secondary velocity modulus recorded for $90° \leqslant \beta \leqslant 270°$ at various times during the acceleration phase. These values increased from $\beta = 270°$ (at the outer wall) to $\beta = 170°$ (near the equatorial plane) and then decreased to
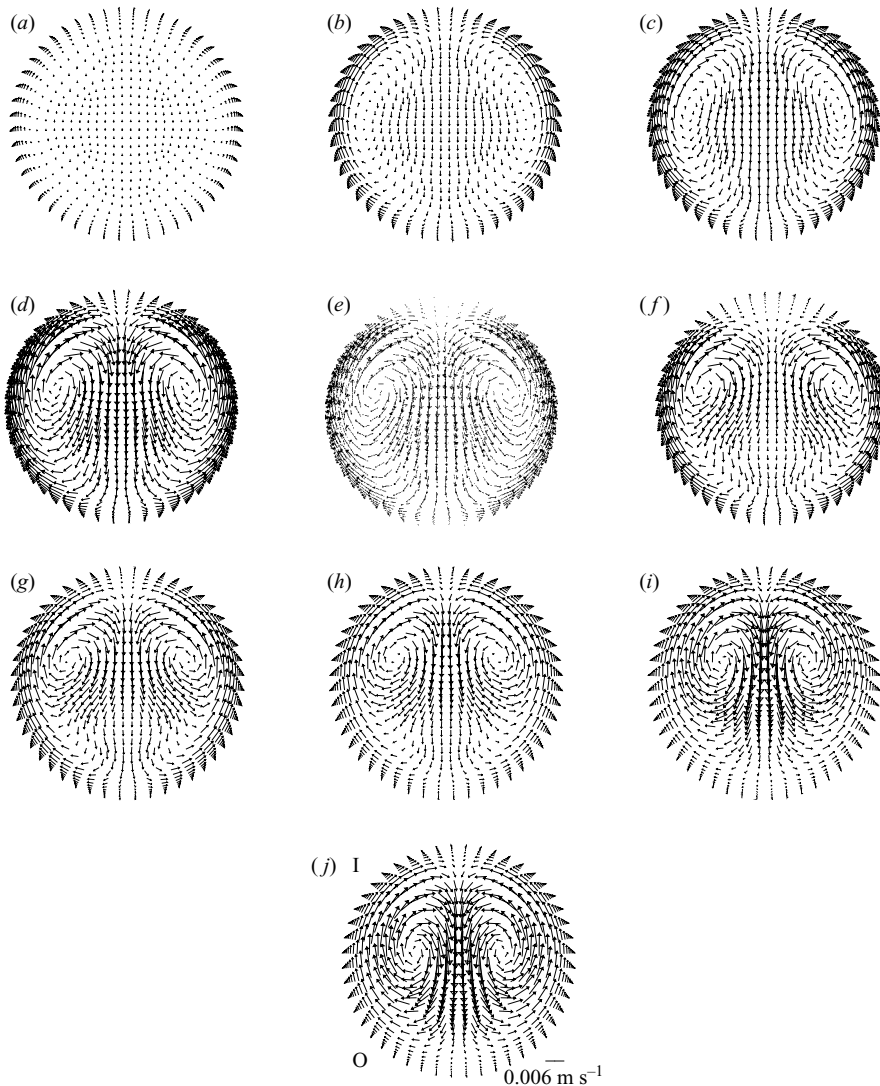
FIGURE 6. Temporal evolution of the velocity vectors in $\theta 90°$ plane. Case 1: $De = 110$, $\alpha = 8$, and (a) $t = 0.2$ s, (b) 0.35 s, (c) 0.5 s, (d) 0.75 s, (e) 0.95 s, (f) 1.35 s, (g) 1.65 s, (h) 1.8 s, (i) 2.3 s, (j) 3 s.

$\beta = 90°$ (at the inner wall). When t is lower than 0.65 s, the maximum value is a crescent function of t.

At the onset of the deceleration phase ($t = 0.7$ s), a secondary dead flow zone developed at the inner wall, which pushed back the circumferential rolls. This dead zone increased up to $t = 1.35$ s. The vortices were mushroom-like in shape.

At the end of the deceleration phase, from $t = 1.6$ to 1.8 s, the circumferential rolls again reached the inner wall, supplying the central jet. The flow rate oscillated around zero and secondary vortices developed in the whole cross-section. Their cores moved towards the outer wall and towards the symmetry plane. These structures are comparable to those observed in the case of a steady flow.
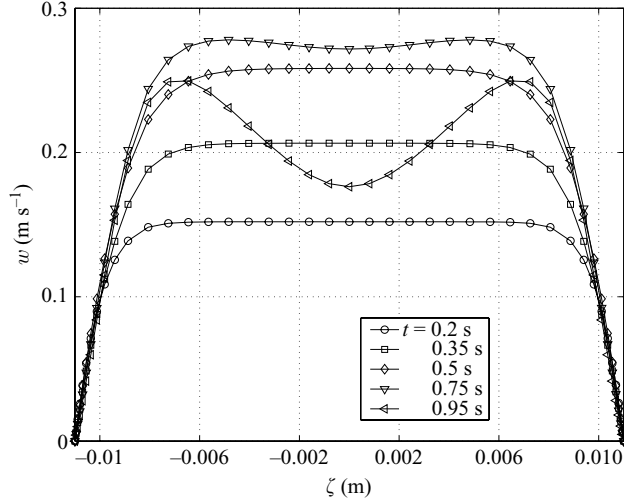
FIGURE 7. Axial velocity profiles, $\theta = 90°$ plane, perpendicular diameter, case 1: $De = 110$, $\alpha = 8$, $0.2 \leqslant t \leqslant 0.95$ s.

Figure 11 shows the decrease in the maximum of the secondary velocity modulus occurring at $90° \leqslant \beta \leqslant 125°$. This decrease was correlated with the occurrence of the secondary dead flow zone at the inner wall.

Subsequently, the flat velocity profiles disappeared and were replaced by the M-shaped axial velocity profiles along the perpendicular diameter (figure 7, $t \geqslant 0.75$ s) associated with mushroom vortices. Along the transverse diameter (figure 8(b), $t \geqslant 0.75$ s), the axial velocity profiles hollowed out close to the inner wall resulting in a decrease in the velocity values until negative values were reached at $t = 1.35$ s.

In case 2 (figure 12), the frequency parameter and the systolic time T_s are the same as in case 1, but the Dean number value is twice as high. The flow rate waveforms show similar acceleration slopes during the early acceleration phase, but very different deceleration slopes (figure 3). Therefore the structures which develop during most of the acceleration phase $0 \leqslant t \leqslant 0.55$ s, are similar to those observed in case 1 but during the deceleration phase a diffrent process occurs.

At $t = 0.8$ s, due to the presence of a strong radial pressure gradient close to the symmetry plane, the vortices are pushed against the lateral walls, so that there is no significant secondary structure at the tube centre. The jet-like motion described in case 1 suddenly stops. This process leads ($0.85 \leqslant t \leqslant 1.1$ s) to a deformed Dean circulation at $\theta = 60°$ (see figure 13), which evolves to an circulation intermediate between the Dean and Lyne ones, at $\theta \geqslant 90°$ (according to the system of classification proposed by Sudo et al. 1992). This is characterized by an additional pair of vortices rotating in the opposite direction to the two primary ones and by undulating axial velocity profiles along the perpendicular diameter (figure 14, $t \geqslant 0.8$ s). The secondary flow structure therefore depends on the position in the bend of the cross-section.

Figure 15 shows the velocity vectors observed in case 5 ($\alpha = 21.5$, $De = 423$). The key factor here is the high value of the frequency parameter leading to a quasi-potential flow during the acceleration ($t \leqslant 0.7$ s). The viscous layer is very thin. Blunt-shaped profiles (figure 16) are observed during this phase along the perpendicular diameter.
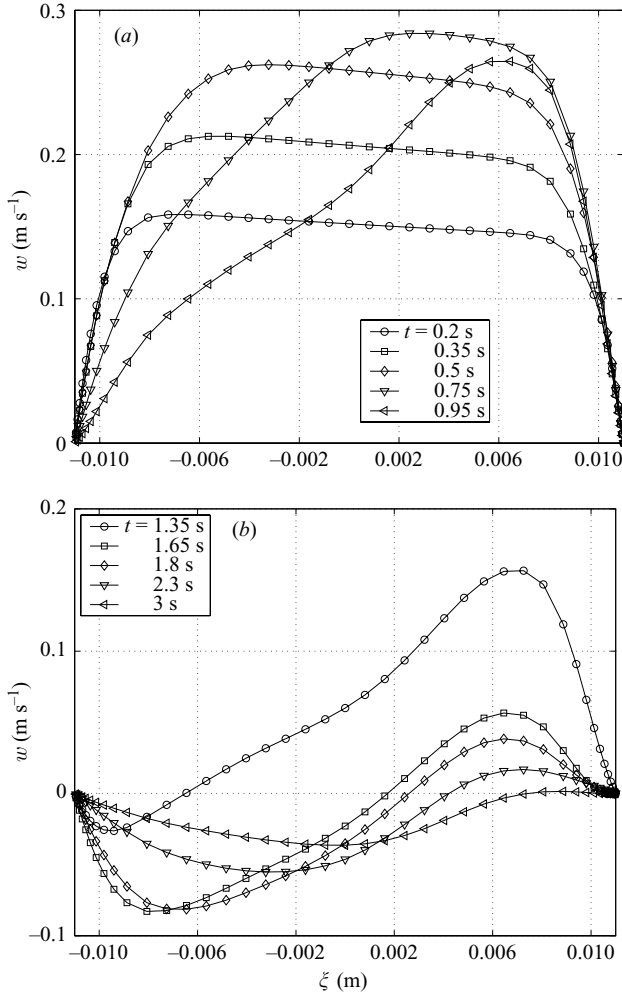
FIGURE 8. Axial velocity profiles, $\theta = 90°$ plane, transverse diameter, case 1: $De = 110$, $\alpha = 8$, and (a) $0.2 \leqslant t \leqslant 0.95$ s, (b) $1.35 \leqslant t \leqslant 3$ s.

The vortices which develop during the deceleration phase are comparable to those observed in case 1, but are more pronounced due to the Dean number value (423 versus 110).

Figure 17 shows a comparison of the secondary structures resulting from the computations with those obtained using flow visualizations in case 3 ($De = 346$, $\alpha = 10.95$). These visualizations are in line with those observed by Pascal-Mousselard & Pelissier (1998) at our laboratory and show good agreement. At this intermediate regime (Sudo *et al.* 1992), in between Dean and Lyne circulation, the most interesting feature as shown in case 2 is the secondary flow behaviour observed during the deceleration phase, where the jet-like motion and the generation of Lyne vortices have a stopping effect.

From this secondary flow pattern analysis, it can be clearly seen that the various acceleration and deceleration times used yielded different vortices patterns, and that the flow waveform therefore plays an important part.
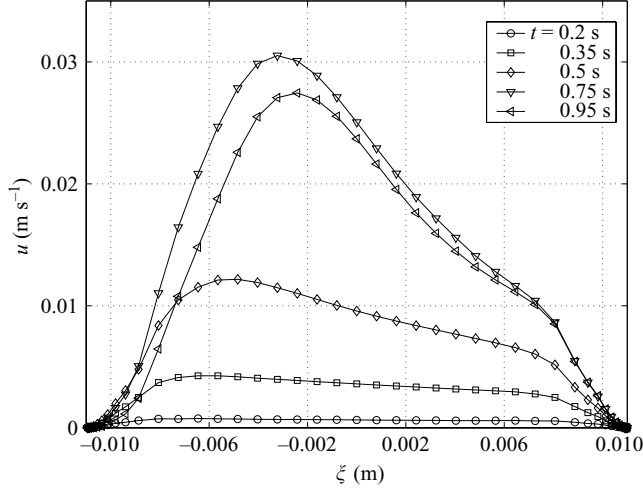
FIGURE 9. Radial velocity profiles, $\theta = 90°$ plane, transverse diameter, case 1: $De = 110$, $\alpha = 8$, $0.2 \leqslant t \leqslant 0.95$ s.
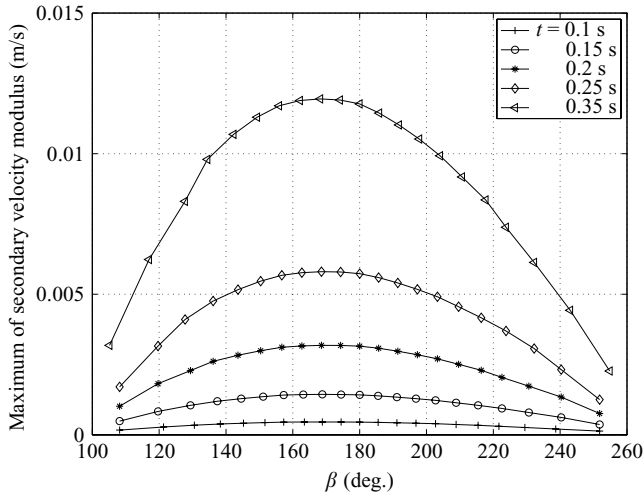

FIGURE 10. Evolution of the maximum secondary velocity modulus versus β during acceleration, $\theta = 90°$ plane, case 1: $De = 110$, $\alpha = 8$.

The frequency parameter referred to the flow period therefore does not suffice to describe the flow behaviour. The time scales associated with the acceleration or the deceleration are key parameters, regardless of the time period. Similar attempts made by Komai & Tanishita (1997) to define an intermediate frequency parameter referred to the systolic time were in agreement with this conclusion. In fact, the acceleration time and deceleration time can be very different without any change in the total systolic time T_s, but when the respective slopes change, which affects the secondary flow structures.

3.3. *Quantitative insight into secondary flow generation mechanisms*

To explain the main features of the secondary flows observed in both cases 2 and 3 quantitatively, we compute the main terms of the radial component of the
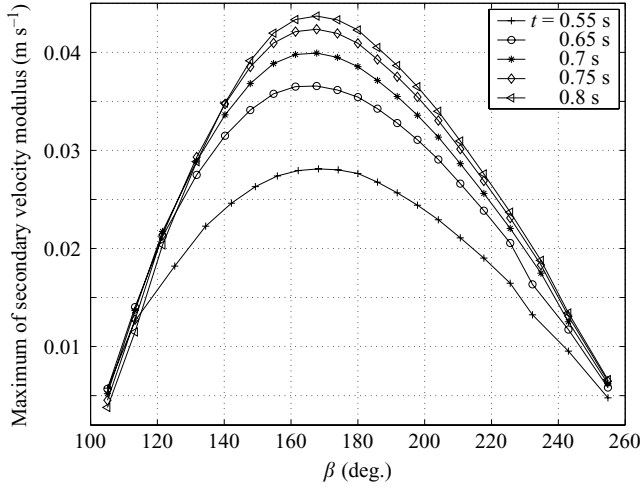
FIGURE 11. Evolution of the maximum secondary velocity modulus versus β during deceleration, $\theta = 90°$ plane, case 1: $De = 110$, $\alpha = 8$.

Navier–Stokes equation in the toroïdal coordinate system along the transverse diameter using the numerical results obtained in case 2 and taking the $\theta = 90°$ plane (figure 2). Using these coordinates, the centrifugal force term is obtained explicitly. In view of the symmetry plane along the transverse diameter, the equation can be reduced to

$$\frac{\partial u}{\partial t} + u \frac{\partial u}{\partial r} + \frac{w}{R+r} \left(\frac{\partial w}{\partial \theta} - w \right) = -\frac{1}{\rho} \frac{\partial p}{\partial r} + \nu f_v. \tag{3.1}$$

Assuming that $w/(R+r)\partial w/\partial \theta$ is smaller than $w^2/(R+r)$ and that the viscous term νf_v is negligible except in the Stokes layer, equation (3.1) becomes

$$\frac{\partial u}{\partial t} + u \frac{\partial u}{\partial r} - \frac{w^2}{R+r} \approx -\frac{1}{\rho} \frac{\partial p}{\partial r}. \tag{3.2}$$

Figure 18 plots of all the terms of equation (3.2). The corresponding secondary flow structures are plotted in figures 12 and 13. The following terms are used in these figures:

the radial pressure gradient (RPG): $\partial p/\partial r$;
the centrifugal force (CF): $\rho w^2/(R+r)$;
the spatial inertial force (SIF): $\rho u \partial u/\partial r$;
the temporal inertial force (TIF): $\rho \partial u/\partial t$.

From figure 18, the following three main points emerge: (i) at all the times t considered the values of RPG and CF are in balance near the outer wall; (ii) from $t = 0.35$ to 1.8 s, RPG and CF dominate SIF and TIF; (iii) at $t > 1.8$ s up to the end of the pulse, all the terms of equation (3.2) are of the same order.

More specifically, during the early acceleration phase (figure 18(a), $t = 0.35$ s), we can observe a state of quasi-equilibrium between RPG and CF near the outer and inner walls. CF dominates RPG over a large part of the diameter under consideration. The values of SIF are around zero and those of TIF are very small.

As the acceleration progresses (figure 18(b), $t = 0.55$ s), CF remains higher than RPG only from $\xi = -0.005$ m towards the inner wall ($\xi = -0.011$ m). This evolution is correlated with a large increase in SIF near the inner wall, from 0 up to 500 N m^{-3},

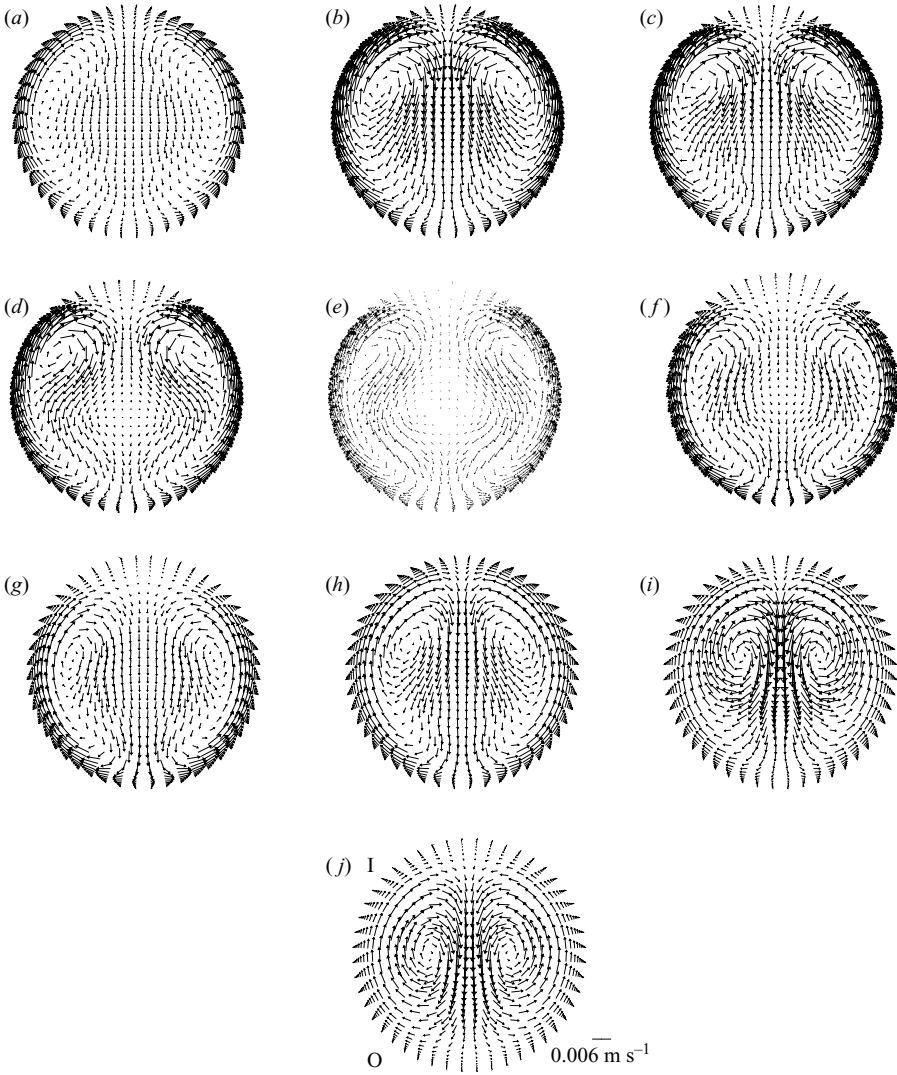FIGURE 12. Temporal evolution of the velocity vectors in $\theta = 90°$ plane. Case 2: $De = 221$, $\alpha = 8.33$, and (*a*) $t = 0.35$ s, (*b*) 0.55 s, (*c*) 0.7 s, (*d*) 0.8 s, (*e*) 0.9 s, (*f*) 1.25 s, (*g*) 1.6 s, (*h*) 1.8 s, (*i*) 2.3 s, (*j*) 3 s.
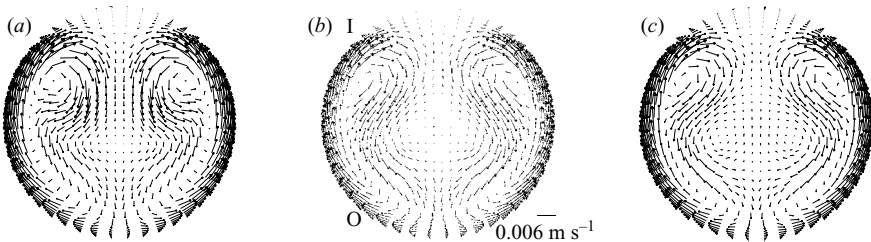

FIGURE 13. Evolution of the velocity vectors in (*a*) $\theta = 60°$, (*b*) 90°, (*c*) 156° planes. Case 2: $De = 221$, $\alpha = 8.33$, $t = 0.9$ s.

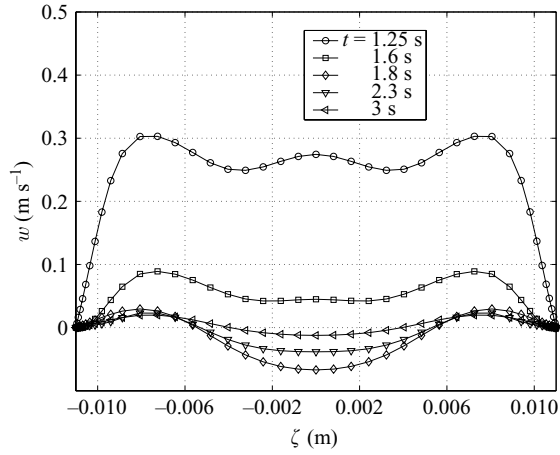FIGURE 14. Axial velocity profiles, $\theta = 90°$ plane, perpendicular diameter, case 2: $De = 221$, $\alpha = 8.33$, $1.25 \leqslant t \leqslant 3$ s.
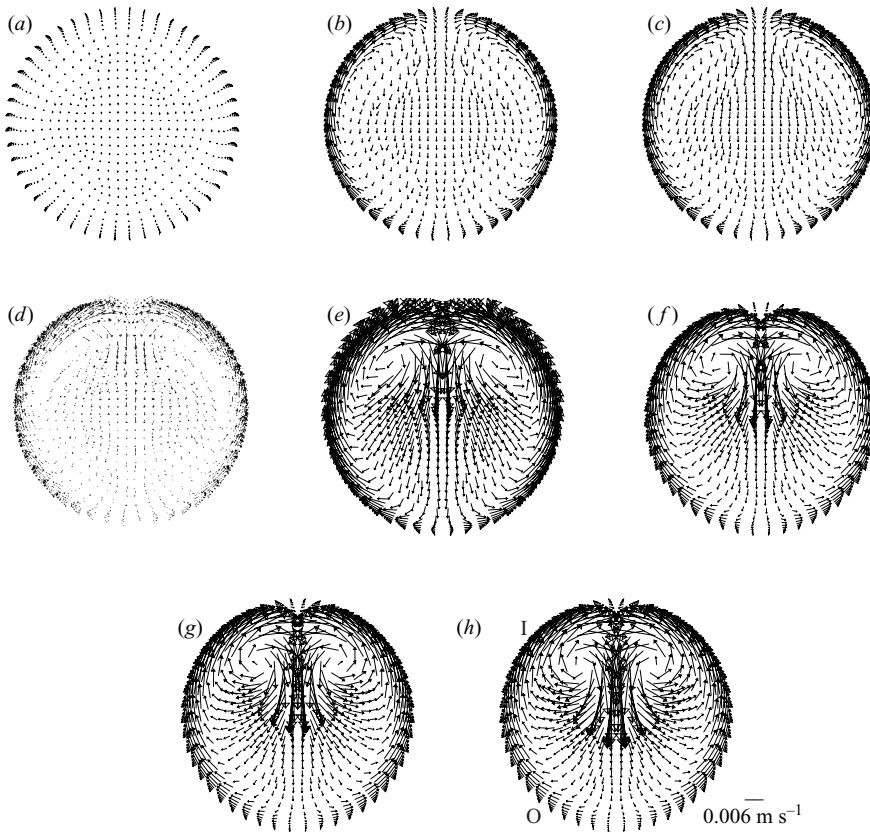

FIGURE 15. Temporal evolution of the velocity vectors in $\theta = 90°$ plane. Case 5: $De = 423$, $\alpha = 21.5$, (*a*) $t = 0.35$ s, (*b*) 0.7 s, (*c*) 0.8 s, (*d*) 1 s, (*e*) 1.3 s, (*f*) 1.6 s, (*g*) 1.7 s, (*h*) 1.8 s.
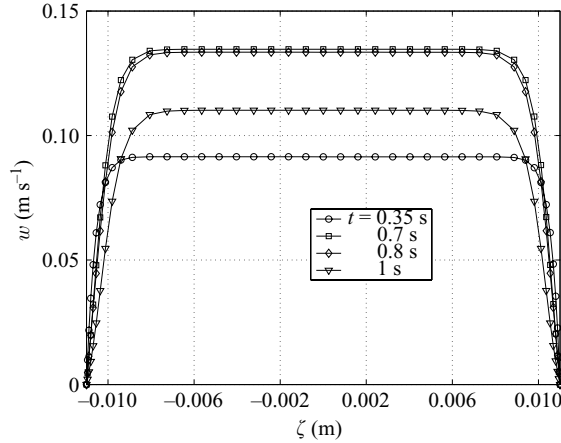
FIGURE 16. Axial velocity profiles, $\theta = 90°$ plane, perpendicular diameter, case 5: $De = 423$, $\alpha = 21.5$.

while TIF still equals zero. A jet-like motion directed towards the outer wall occurs (figure 12, $t = 0.55$ s). From $-0.005 \leqslant \xi \leqslant 0$, the SIF values become negative, and the TIF values become correspondingly positive; FC and RPG are in balance. SIF and TIF control the mechanism of CF and RPG prevalence.

During the deceleration onset (figure 18(c, d), $t = 0.7$ s, $t = 0.8$ s), the TIF values become negative over the whole diameter, the SIF values decrease and RPG is greater than CF over a large part of the diameter. The predominance of RPG over CF corresponds to the stopping of the jet-like motion (figure 13, $t = 0.8$ s).

As the deceleration progresses (figure 18(e, f), $t = 0.9$ s, $t = 1.25$ s), the SIF and TIF values become negligible over the whole diameter. We note the equilibrium existing between RPG and CF.

From $t = 1.6$ s onwards, we note the occurrence of a significant decrease in RPG and CF. At $t = 1.8$ s, all the forces are of the same order.

Finally, during the systolic time T_s the pressure gradient and radial centrifugal forces were found to be several orders of magnitude greater than the spatial and temporal inertial forces. However, the two latter forces seem to completely drive the balance between the pressure gradient and centrifugal forces and hence the flow behaviour, as described above.

4. Conclusion

In the present study, starting/stopping flows in a bend were investigated experimentally and numerically modelled. For the first time, visualizations of the developing secondary flows have been presented with numerical simulations and hot-film velocity measurements. The secondary flow patterns visualized were in good agreement with the computed ones. The hot-film velocity measurements performed along the transverse diameter are also in good agreement with the computed velocities.

Based on these concordant qualitative and quantitative data, it can be concluded that numerical results of this kind can be reliably used to analyse secondary flow dynamics through the velocity and pressure fields occurring in bends.

At some De and α values, the propagation of the vortices from the inner wall towards the outer wall stops. This behaviour has been analysed on the basis of the
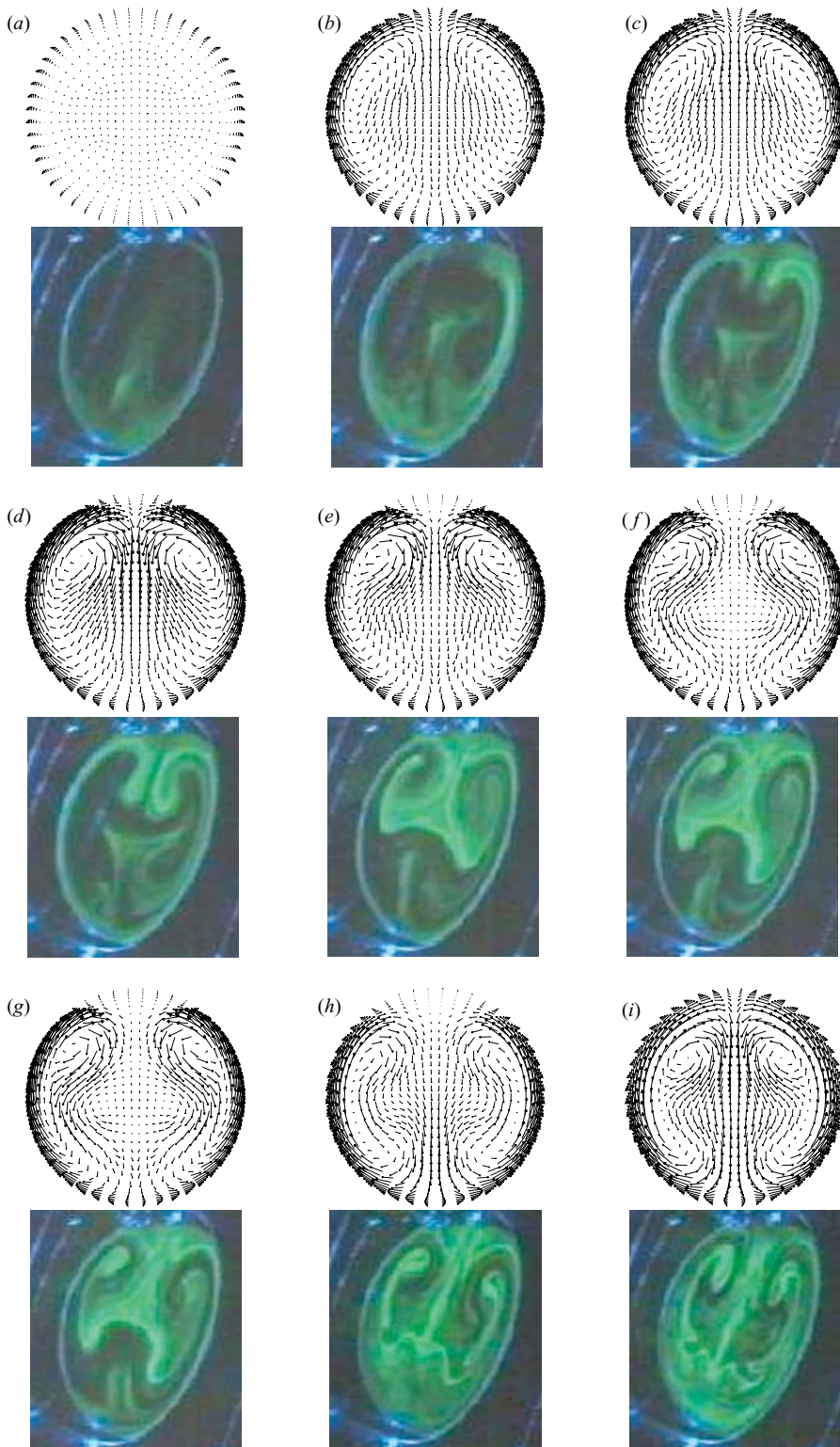
FIGURE 17. Comparison between numerical results and flow visualizations of the secondary flow evolution in the $\theta = 120°$ plane. Case 3: $De = 346$, $\alpha = 10.95$. (*a*) $t = 0.2$ s, (*b*) 0.45 s, (*c*) 0.5 s, (*d*) 0.66 s, (*e*) 0.8 s, (*f*) 0.9 s (*g*) 0.96 s, (*h*) 1.35 s, (*i*) 1.65 s line 3.
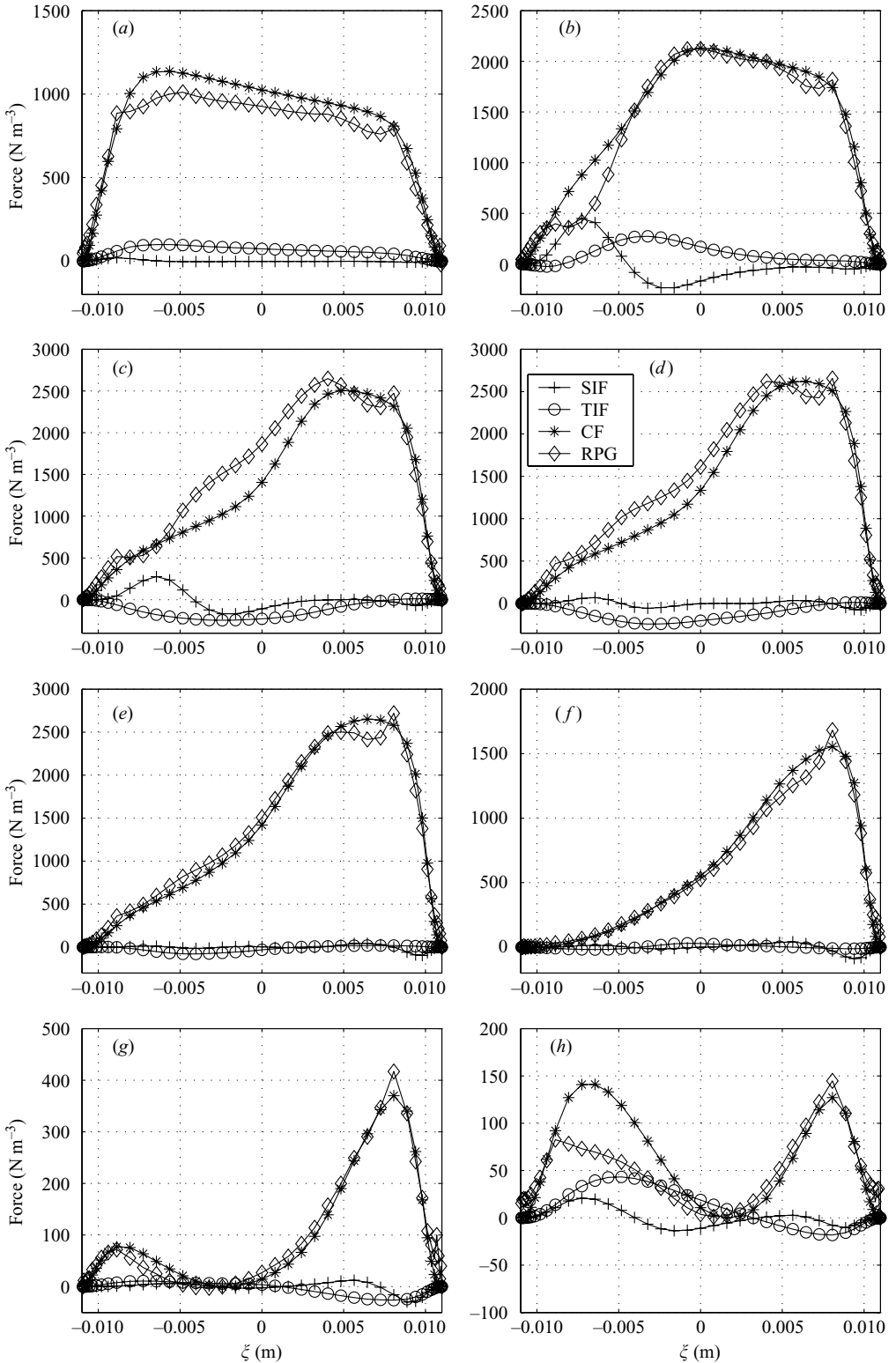
FIGURE 18. Forces, $\theta = 90°$ plane, transverse diameter, Case 2: $De = 221$, $\alpha = 8.33$ and (*a*) $t = 0.35$ s, (*b*) 0.55 s, (*c*) 0.7 s, (*d*) 0.8 s, (*e*) 0.9 s, (*f*) 1.25 s, (*g*) 1.6 s, (*h*) 1.8 s.

main forces involved in the Navier–Stokes equation in a toroïdal coordinate system. When the radial pressure gradient prevails over the centrifugal force a stagnant secondary flow develops and Lyne vortices occur. Finally, the dependence of the secondary flow patterns on the initial conditions is clearly highlighted.

REFERENCES

AVULA, X. 1969 A combined method for determining velocity of starting flow in a long circular tube. *J. Phys. Soc. Japan* **27**, 497–502.

BERGER, S., TALBOT, L. & YAO, L. 1983 Flow in curved pipes. *Annu. Rev. Fluid Mech.* **15**, 461–512.

BERTELSEN, A. 1975 An experimental investigation of low reynolds number secondary streaming effects associated with an oscillating viscous flow in a curved pipe. *J. Fluid Mech.* **70**, 519.

CARO, C., FITZGERALD, J. & SCHROTER, R. 1971 Atheroma and wall shear stress: observation, correlation and proposal of a shear dependent mass transfer mechanism of atherogenesis. *Proc. R. Soc. Lond.* B **177**, 109–159.

CHANDRAN, K. & YEARWOOD, T. 1981 Experimental study of physiological pulsatile flow in a curved tube. *J. Fluid Mech.* **111**, 59–85.

CHANG, L. & TARBELL, J. 1985 Numerical simulation of fully developed sinusoidal and pulsatile (physiological) flow in a curved tubes. *J. Fluid Mech.* **161**, 175–198.

ECKMANN, D. & GROTBERG, J. 1988 Oscillatory flow and mass transport in a curved tube. *J. Fluid Mech.* **188**, 509.

FLUENT 1998 *User' Guide*, vol. 3. Fluent Inc.

FRIEDMAN, M., HUTCHINS, G., BARGERON, C., DETERS, O. & MARK, F. 1981 Correlation of human arterial morphology with hemodynamic measurements in arterail casts. *Trans. ASME: J. Biomech. Engng* **103**, 204–207.

GESSNER, F. 1973 Hemodynamic theories of atherogenesis. *Circ. Res.* **43**.

JØRGENSEN, F. 1971 Directionnal sensitivity of wire and fibre-films probes. *DISA Info.* **11**, 31–37.

KOMAI, Y. & TANISHITA, K. 1997 Fully developed intermittent flow in a curved tube. *J. Fluid Mech.* **347**, 263–287.

KU, D., ZARINS, C., GIDDENS, D. & GLAGOV, S. 1985 Pulsatile flow and artherosclerosis in the human carotid bifurcation: positive correlation between plaque localization and low and oscillating shear stress. *Arteriosclerosis* **5**.

LYNE, W. 1971 Unsteady viscous flow in a curved pipe. *J. Fluid Mech.* **45**, 13.

MULLIN, T. & GREATED, C. 1980 Oscillatory flow in curved pipes. Part 2. The fully developed case. *J. Fluid Mech.* **98**, 397–416.

MUNSON, B. 1975 Experimental results for oscillating flow in a curved pipe. *Phys. Fluids* **18,12**, 1607–1609.

NARUSE, T. & TANISHITA, K. 1996 Large curvature effect in curved pipes. *J. Fluid Mech.* **118**, 180–186.

PARKER, K. 1977 *Instability in Arterial Blood Flow in Cardiovascular Flow Dynamics and Measurements*. University Park Press.

PASCAL-MOUSSELARD, A. & PELISSIER, R. 1998 Secondary pattern in a bend for oscillatory and physiological flow conditions. In *Abstracts of the Third World Congress of Biomechanics, p 231* (ed. T. N. Y. Matsuzaki & E. Tanaka). Sapporo, Japan.

PEDLEY, T. 1980 *The Fluid Mechanics of Large Blood Vessels*. Cambridge University Press.

PELISSIER, R. 1972 Mouvement pseudo périodique d'une colonne liquide-critères de transition. PhD thesis, Université Aix Marseille II, France.

RINDT, C., STEENHOVEN, A. V., JANSSEN, J. & VOSSERS, G. 1991 Unsteady entrance flow in a 90° curved tube. *J. Fluid Mech.* **226**, 445.

SUDO, K., SUMIDA, M. & YAMANE, R. 1992 Secondary motion of fully developed oscillatory flow in a curved pipe. *J. Fluid Mech.* **237**, 189–208.

TALBOT, L. & GONG, K. 1983 Pulsatile entrance flow in curved pipes. *J. Fluid Mech.* **127**, 1–25.

WEINBAUM, S. & PARKER, K. 1975 The laminar decay of suddenly blocked channel and pipe flows. *J. Fluid Mech.* **69**, 729–752.

YEARWOOD, T. & CHANDRAN, K. 1984 Physiological pulsatile flow experiments in a model of the human aortic arch. *J. Biomech.* **15,9**, 683–704.

ZALOSH, R. & NELSON, N. 1973 Pulsating flow in a curved tube. *J. Fluid Mech.* **59**, 693.